GEOPHYSICS, VOL. 57, NO. 10 (OCTOBER 1992); P. 1294–1306, 14 FIGS.

Array responses for plane and spherical incidence

Guy M. Cross*

ABSTRACT

The design of array filters for attenuation of source-generated seismic noise is founded, almost without exception, on the assumption of plane-wave incidence. We examine the theoretical limitations of this assumption and assess their practical significance. A time-domain array response is developed, incorporating spherical wavefront geometry and divergence. Departures from conventional plane-wave response are related to systematic differences between the spectral composition of respective waveforms within the array's aperture. The study also develops a hybrid-array response based on a modified plane-wave assumption, retaining plane wavefront geometry but incorporating a model-consistent approximation to spherical divergence. Deviations between the spherical-wave response and those arising under plane-wave assumptions are analyzed in terms of effective implementation errors required to compensate. Analysis reveals that the magnitude of these effective deviations can significantly exceed those expected for actual implementation errors. Findings establish that errors stemming from a plane-wave approximation are controlled by the ratio of reflector depth to aperture width and diminish as the distance between the source and array midpoint becomes large compared with the former parameters.

INTRODUCTION

The filtering properties of receiver arrays are well understood and typically characterized assuming plane-wave incidence over the length of the array (e.g., Parr and Mayne, 1955; Holzman, 1963; Dobrin, 1976). As the scale of seismic application decreases, however, it is useful to review the basis of this assumption and assess both its theoretical and practical limitations. To this end, the apparent surface wavefield arising for a monochromatic spherical wave is compared with that predicted for plane-wave incidence. Corresponding apparent wavenumber distributions facilitate an initial assessment of the plane-wave approximation. Subsequently, we examine the influence of systematic deviations between these apparent wavefields on the output of a line array of equispaced, uniformly effective receivers.

Viewed as a spatial filter, the array's response is determined completely by the number of elements, their relative weighting, and spatial distribution. The relative attenuation of plane and spherically incident waves depends on the spectral composition of associated apparent waveforms within the aperture of the array. Alternatively, array attenuation properties can be related to the time-dependent variability of these apparent waveforms and, consequently, it is also useful to characterize the array's time-domain response. In addition to the distribution and weighting of individual elements, the time-domain impulse response incorporates wavefront geometry and spatial amplitude dependence. As a result, distinct responses arise in connection with plane and spherical incidence. Examination of array filters in both spatial and temporal contexts reveals that the actual attenuation of a spherical wave can deviate appreciably from that predicted assuming plane incidence.

Although the following analysis is illustrated on a scale reflecting archaeological application, the findings are of a general nature and may be appropriately scaled as necessary.

APPARENT WAVEFIELDS

Consider a monochromatic spherical wave of the form

$$\psi_s(x, y, z, t) = \frac{U_0}{4\pi r} H\left[t - \frac{r}{v}\right] \cos\left[2\pi k(r - vt)\right] \quad (1)$$

emanating from an image source located at x_s, y_s, z_s within a homogeneous, isotropic half-space having velocity v. Here, $U_0 = 4\pi u_0^2$ denotes the surface displacement of a point source having initial outward radial displacement u_0, k is the linear wavenumber, $r = [(x - x_s)^2 + (y - y_s)^2 + (z - z_s)^2]^{1/2}$ is the distance from the source to an arbitrary location x, y, z and

Manuscript received by the Editor October 4, 1991; revised manuscript received April 7, 1992.
*Geophysics and Astronomy, University of British Columbia, Vancouver, B.C. V6T 1Z4, Canada.

$$H[\tau] = \begin{cases} 0, & \tau < 0; \\ 1/2, & \tau = 0; \\ 1, & \tau > 0 \end{cases}$$

is the Heaviside step function. Spatial coordinates are specified in relation to a rectangular coordinate system having its origin at the surface and z increasing with depth as illustrated in Figure 1.

Neglecting free surface interaction and given that sufficient time has elapsed for incident energy to extend over the region of interest, we take $H[t - r/v] = 1$, obtaining

$$\psi_s(x, y) = \frac{U_0}{4\pi r} \cos [\phi_s(x, y)] \tag{2}$$

for the instantaneous apparent wavefield detected by omnidirectional sensors on the surface ($z = 0$). The associated phase function is

$$\phi_s(x, y) = 2\pi k(r - vt), \tag{3}$$

where $r = [(x - x_s)^2 + (y - y_s)^2 + z_s^2]^{1/2}$. Neglecting the minor influence of spherical divergence, the local apparent wavenumber in the x-direction follows from equation (3) as

$$\tilde{k}_{s,x}(x, y) = \frac{1}{2\pi} \frac{\partial \phi_s(x, y)}{\partial x} = \frac{k}{r}(x - x_s). \tag{4}$$

A similar expression arises for the local apparent wavenumber in the y-direction

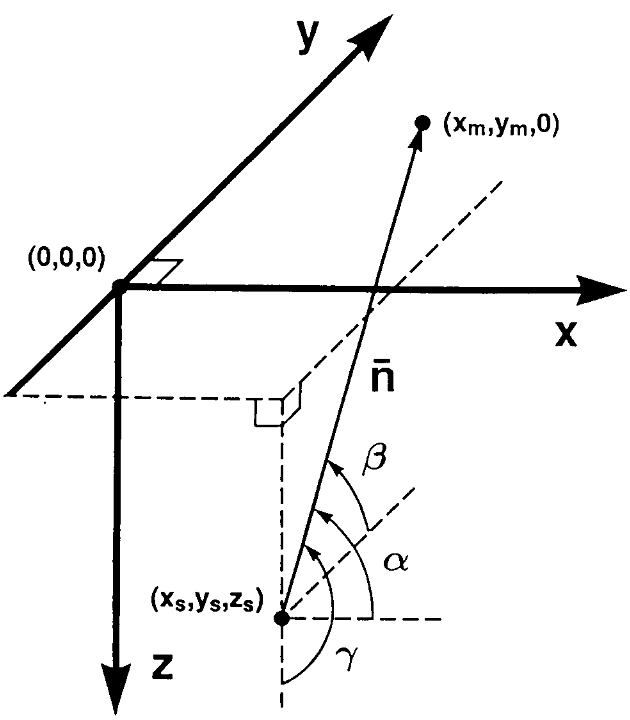

FIG. 1. Rectangular coordinate system for analysis of plane and spherical wavefronts emanating from an image source at x_s, y_s, z_s. Propagation vector **n** is normal to plane wavefronts incident on the surface at x_m, y_m and has direction angles α, β, γ.

$$\tilde{k}_{s,y}(x, y) = \frac{1}{2\pi} \frac{\partial \phi_s(x, y)}{\partial y} = \frac{k}{r}(y - y_s). \tag{5}$$

The associated plane-wave system incident at some point x_m, y_m on the surface is given by

$$\psi_p(x, y, z, t) = \frac{U_0}{4\pi r \cos\theta} H\left[t - \frac{r\cos\theta}{v}\right] \times \cos\{2\pi k[\ell(x - x_s) + m(y - y_s) + n(z - z_s) - vt]\}, \tag{6}$$

where

$$\ell = \cos\alpha = (\mathbf{n} \cdot \mathbf{u}_x)/|\mathbf{n}| = (x_m - x_s)/|\mathbf{n}|$$
$$m = \cos\beta = (\mathbf{n} \cdot \mathbf{u}_y)/|\mathbf{n}| = (y_m - y_s)/|\mathbf{n}|$$
$$n = \cos\gamma = (\mathbf{n} \cdot \mathbf{u}_z)/|\mathbf{n}| = -z_s/|\mathbf{n}|$$

are direction cosines for the propagation direction vector **n** joining the source with the point of incidence as depicted in Figure 1 with $\mathbf{u}_x$, $\mathbf{u}_y$, and $\mathbf{u}_z$ denoting unit vectors in the positive x-, y-, and z-directions. Note that as a local approximation to the spherical wave, we take plane-wave amplitude and onset to depend on normal distance from the source $r\cos\theta = (\mathbf{r} \cdot \mathbf{n})/|\mathbf{n}|$, where θ is the angle between the propagation direction vector and a position vector **r**, locating an arbitrary point x, y, z. This amplitude dependence is a logical modification to the conventional definition of plane waves, providing a reasonable approximation to the effect of spherical divergence in the vicinity of incidence while retaining plane-wave geometry. Where it is necessary to differentiate between this form and the conventional constant amplitude plane wave, the former is referred to as a modified plane wave.

Assuming, again, that sufficient time has elapsed to set $H[t - r\cos\theta/v] = 1$, the instantaneous apparent surface wavefield in the vicinity of incidence is

$$\psi_p(x, y) = \frac{U_0}{4\pi r\cos\theta} \cos[\phi_p(x, y)], \tag{7}$$

where

$$\phi_p(x, y) = 2\pi k[\ell(x - x_s) + m(y - y_s) - nz_s - vt] \tag{8}$$

is the associated phase function. Ignoring the minor influence of gradual amplitude variation, the corresponding apparent local wavenumber distributions are

$$\tilde{k}_{p,x}(x, y) = \frac{1}{2\pi} \frac{\partial \phi_p(x, y)}{\partial x} = k\cos\alpha \tag{9}$$

and

$$\tilde{k}_{p,y}(x, y) = \frac{1}{2\pi} \frac{\partial \phi_p(x, y)}{\partial y} = k\cos\beta. \tag{10}$$

As an example, Figure 2 displays apparent surface wavefields computed using equations (2) and (7) for spherical and plane-waves incident at a point $x_m = 1.7$ m, $y_m = 0.0$ m on the surface. Here, the source is located beneath the origin at

$x_s = 0.0$ m, $y_s = 0.0$ m, $z_s = 2.0$ m and the incident wavenumber is $k = 2.0\ \mathrm{m}^{-1}$, implying a wavelength of 0.5 m. A measure of the difference between apparent wavefields for plane and spherical incidence is obtained by comparing the corresponding apparent wavenumber distributions defined by equations (4), (5), (9), and (10). Local apparent wavenumbers arising for the spherically incident wave are depicted in Figure 3 and exhibit significant departures from the constant values of $\bar{k}_{p,x} \approx 1.3\ \mathrm{m}^{-1}$ and $\bar{k}_{p,y} = 0.0\ \mathrm{m}^{-1}$ for plane-wave incidence. In the following section, a connection is made between the nature of these deviations and the attenuation properties of spatial arrays.

SPATIAL ARRAY FILTERS

In general, the spatial impulse response of a two-dimensional (2-D) receiver array can be described as

$$a(x, y) = \frac{1}{N} \sum_{j=1}^{N} w_j \delta(x - x_j, y - y_j), \tag{11}$$

where N is the number of elements, x_j, y_j are the coordinates of the jth element, w_j is an associated weighting coefficient, and $\delta(x, y)$ is the 2-D Dirac delta function. The weighting coefficient incorporates factors including the sensitivity, directionality, coupling, and electrical connection of the jth receiver. If coordinates x_m, y_m specify the array midpoint, its instantaneous output is $s(x_m, y_m)$, where

$$s(x, y) = a(x, y) ** \psi(x, y). \tag{12}$$

Here, $\psi(x, y)$ represents the instantaneous surface wavefield as described by equations (2) and (7) and ** denotes 2-D convolution. Alternatively, the filtering process can be described as

$$S(k_x, k_y) = A(k_x, k_y)\Psi(k_x, k_y) \tag{13}$$

where $A(k_x, k_y)$ is the array's transfer function defined by

$$A(k_x, k_y) = \int_{-\infty}^{+\infty}\int_{-\infty}^{+\infty} a(x, y) e^{-i2\pi(k_x x + k_y y)}\, dx\, dy \tag{14}$$

and $\Psi(k_x, k_y)$ is the wavenumber-domain representation of $\psi(x, y)$ given by its 2-D Fourier transform with respect to spatial variables x and y. The array output $s(x_m, y_m)$ is obtained from the inverse Fourier transform

$$s(x, y) = \int_{-\infty}^{+\infty}\int_{-\infty}^{+\infty} S(k_x, k_y) e^{i2\pi(k_x x + k_y y)}\, dk_x\, dk_y. \tag{15}$$

For the sake of illustration, further treatment assumes a line array deployed along the x-axis, having an odd number of equispaced elements and unit weighting.

On invoking the foregoing conditions, the array's spatial impulse response can be written as

$$a(x) = \frac{1}{N} \sum_{j=-(N-1)/2}^{(N-1)/2} \delta(x - j\Delta x), \tag{16}$$

where Δx is a constant denoting the distance between adjacent receivers. The associated transfer function is

$$A(k_x) = |A(k_x)| e^{i\Theta(k_x)} = \frac{1}{N} \sum_{j=-(N-1)/2}^{(N-1)/2} e^{-i2\pi k_x j \Delta x}, \tag{17}$$

where

$$|A(k_x)| = \frac{1}{N} \left| \frac{\sin(N\pi k_x \Delta x)}{\sin(\pi k_x \Delta x)} \right|$$

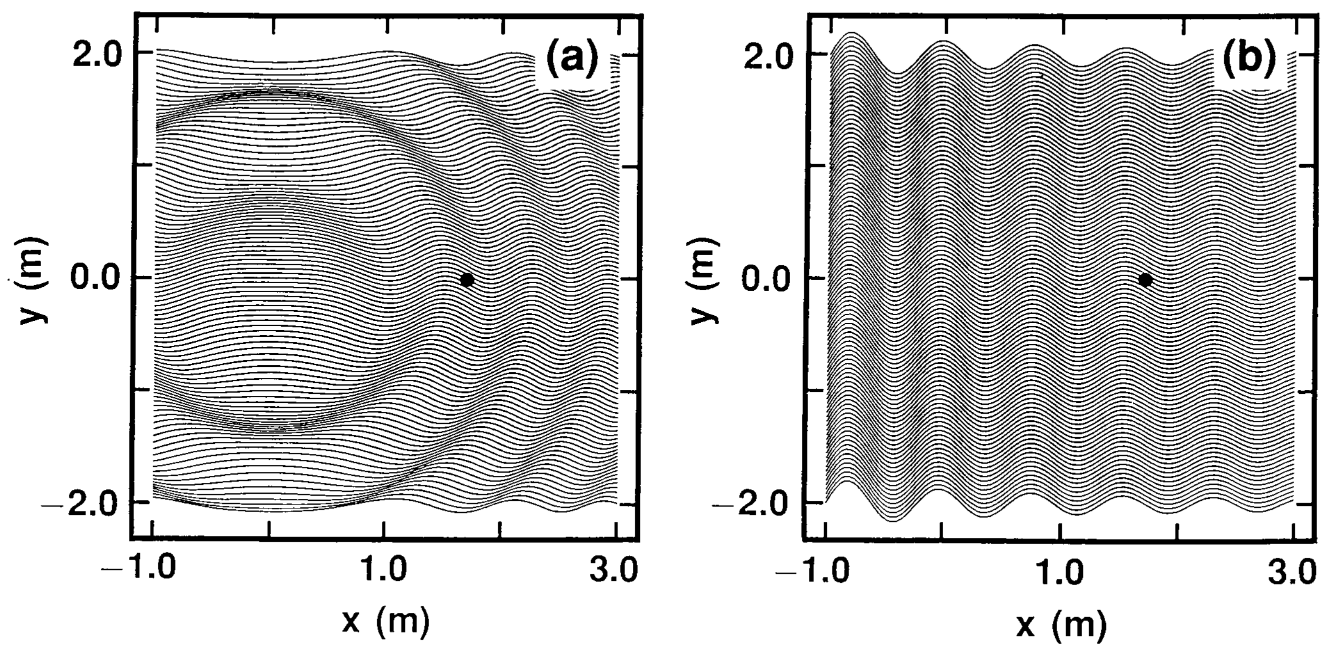

FIG. 2. (a) Apparent surface wavefields arising for a monochromatic spherical wave having its image source at depth $z_s = 2.0$ m beneath the origin. (b) Associated apparent wavefield assuming modified plane incidence at $x_m = 1.7$ m, $y_m = 0.0$ m as indicated by solid circles. Incident waves have $\lambda = 0.5$ m.

and

$$\Theta(k_x) = \begin{cases} 0 \pm n2\pi, & \sin(N\pi k_x \Delta x)/\sin(\pi k_x \Delta x) \geq 0; \\ \pi \pm n2\pi, & \sin(N\pi k_x \Delta x)/\sin(\pi k_x \Delta x) < 0 \end{cases}$$

are, respectively, the corresponding amplitude and phase spectra depicted in Figure 4 for the case $N = 7$. Note that the arbitrary constant $\pm n2\pi$ allows some latitude in displaying an acceptable phase spectrum. In addition to being an odd function, as required, the spectrum in Figure 4 is physically plausible as we shall find in a later section. It is also important to note that the receiver interval imposes a Nyquist wavenumber of $k_N = 1/(2\Delta x)$ so that $k_N \Delta x = 0.5$. Wavenumbers exceeding k_N are spatially aliased in the process of filtering.

ATTENUATION OF APPARENT WAVEFIELDS

It is evident from the foregoing analysis that the relative attenuation of plane and spherically incident waves depends on the apparent wavenumber compositions of the respective surface wavefields. Consider, for example, apparent waveforms arising along the x-axis in Figure 2. These waveforms are depicted in Figure 5 together with a cross-section through the earth model illustrating plane and spherical wavefront systems. It can be seen from this diagram that, despite gradual amplitude variation, modified plane-wave incidence yields a spatial waveform having a practically constant apparent wavelength

$$\tilde{\lambda}_{p,x} = \frac{\lambda}{\cos \alpha} \tag{18}$$

consistent with equation (9), where $\lambda = 1/k$ is the wavelength of the incident wave. In contrast, spherical incidence yields a spatial waveform having variable apparent wavelength

$$\tilde{\lambda}_{s,x}(x) = \lambda \left[1 + \left(\frac{z_s}{x}\right)^2\right]^{1/2} \tag{19}$$

as predicted by equation (4) for $x_s = 0$. Consequently, a finite-length array deployed along the x-axis with midpoint at x_m samples a spatial waveform comprised of a continuous band of apparent wavenumbers rather than the single, unique wavenumber implied by plane incidence. Notice that in setting $x = x_m$, equation (19) reduces to equation (18) and, thus, there is exact agreement between the corresponding spatial waveforms at the point of incidence as illustrated in Figure 5. Relative attenuation of plane and spherically incident wave depends on the nature of the departure of $\tilde{\lambda}_{s,x}(x)$ from $\tilde{\lambda}_{p,x} = \tilde{\lambda}_{s,x}(x_m)$ over the aperture of the array. If the departure is insignificant, it is appropriate to assume plane-wave incidence and the corresponding attenuation may be read directly from the array's amplitude spectrum for $\tilde{\lambda}_{p,x}$. If, however, local apparent wavenumbers predicted by

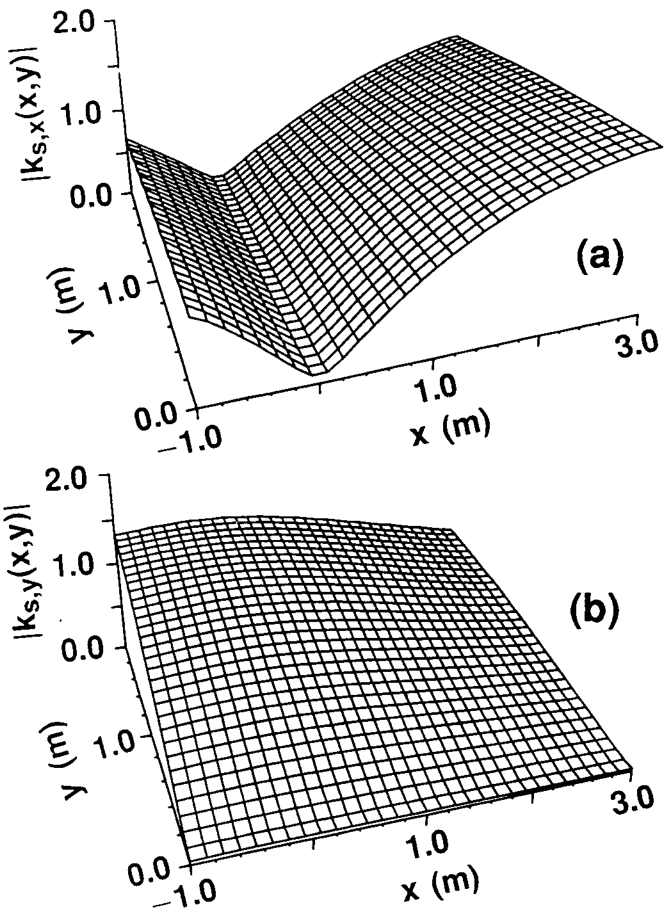

FIG. 3. Local apparent wavenumber distributions in the (a) x-direction and (b) y-direction associated with the apparent surface wavefield in Figure 2a. Corresponding apparent wavenumbers for plane incidence are, respectively, $\tilde{k}_{p,x} \approx 1.3$ and $\tilde{k}_{p,y} = 0.0$ m^{-1}. Incident waves have $k = 1/\lambda = 2.0$ m^{-1}.

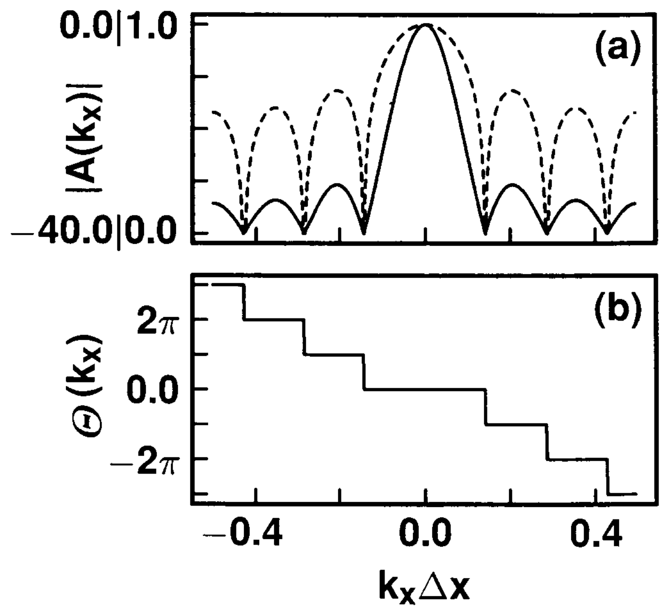

FIG. 4. (a) Amplitude and (b) phase spectra for a linear receiver array having seven equispaced and uniformly effective elements. The ordinate is the apparent wavenumber scaled by the detector interval Δx. The dashed spectrum indicates attenuation on a decibel scale truncated at -40.0 dB. The phase angle is measured in radians.

equation (19) differ significantly from $\tilde{\lambda}_{p,x}$, relative attenuation depends on the distribution of $\tilde{\lambda}_{s,x}(x)$ about $\tilde{\lambda}_{p,x}$, as well as the array's response characteristics.

Figure 5 illustrates that $\tilde{\lambda}_{s,x}(x)$ is less than $\tilde{\lambda}_{p,x}$ for $x > x_m$ and exceeds $\tilde{\lambda}_{p,x}$ for $x < x_m$. It is also evident that the absolute difference $|\tilde{\lambda}_{s,x}(x_m - \varepsilon) - \tilde{\lambda}_{p,x}|$ is greater than $|\tilde{\lambda}_{s,x}(x_m + \varepsilon) - \tilde{\lambda}_{p,x}|$ where ε is a positive constant and $x_m \pm \varepsilon \geq 0$. These observations are extended in Figure 6 by computing the average apparent wavenumber, $\bar{k}_{s,x}(x_m)$, over a range of fixed length windows as a function of the midpoint x_m. The mean value theorem for integrals yields

$$\bar{k}_{s,x}(x_m, y) = \frac{1}{2\delta} \int_{x_m - \delta}^{x_m + \delta} \tilde{k}_{s,x}(x, y)\, dx, \tag{20}$$

where $\delta = [(N - 1)\Delta x]/2$ is half the aperture length of an equispaced linear array having N elements separated by an interval Δx. Substituting equation (4) with $x_s = 0$ and evaluating, yields the following expression for the average apparent wavenumber along the x-axis

$$\bar{k}_{s,x}(x_m) = \frac{k(x_m^2 + z_s^2)^{1/2}}{2\delta} \left[\left(1 + \frac{2x_m\delta + \delta^2}{x_m^2 + z_s^2} \right)^{1/2} - \left(1 - \frac{2x_m\delta - \delta^2}{x_m^2 + z_s^2} \right)^{1/2} \right]. \tag{21}$$

Finally, on expanding the square roots in the previous expression and retaining terms to second order in δ, we obtain the approximate relation

$$\bar{k}_{s,x}(x_m) \approx \tilde{k}_{s,x}(x_m) - \frac{k x_m \delta^2}{2(x_m^2 + z_s^2)^{3/2}} \left[1 - \frac{x_m^2}{x_m^2 + z_s^2} \right]. \tag{22}$$

Although, strictly speaking, this approximation is only valid for $\delta \ll (x_m^2 + z_s^2)^{1/2}$, it provides useful insight on the relation between local and average apparent wavenumbers. As expected, $\lim_{\delta \to 0} \bar{k}_{s,x}(x_m) = \tilde{k}_{s,x}(x_m)$. More significantly, since the second term in equation (22) is positive valued, the magnitude of the average wavenumber impinging on a finite-length array is always less than that predicted for plane incidence. This conclusion is illustrated in Figure 6a where the average apparent wavenumber computed using equation (21) is displayed, together with the local plane-wave value ($\delta = 0$), as functions of x_m for fixed window lengths between 0.5 and 3.0 m. We observe that the difference $\tilde{k}_{s,x}(x_m) - \bar{k}_{s,x}(x_m)$, displayed in Figure 6b, is in all cases positive. The approximate expression (22) yields nearly indistinguishable results for $\delta \leq 1.0$ m.

Given the nominally low pass nature of receiver arrays, the foregoing conclusion suggests that the actual attenuation of spherical waves is less than that predicted assuming plane incidence. As demonstrated in the previous section and illustrated in Figure 4, however, the amplitude spectra of spatial filters are generally multilobed. Consequently, although the envelope of these lobes decreases monotonically as the Nyquist wavenumber is approached, the attenuation can be high pass in nature over a limited band. Strictly speaking, the array output at an arbitrary midpoint x_m depends on the full wavenumber spectrum comprising the waveform within the array's aperture. But, having issued

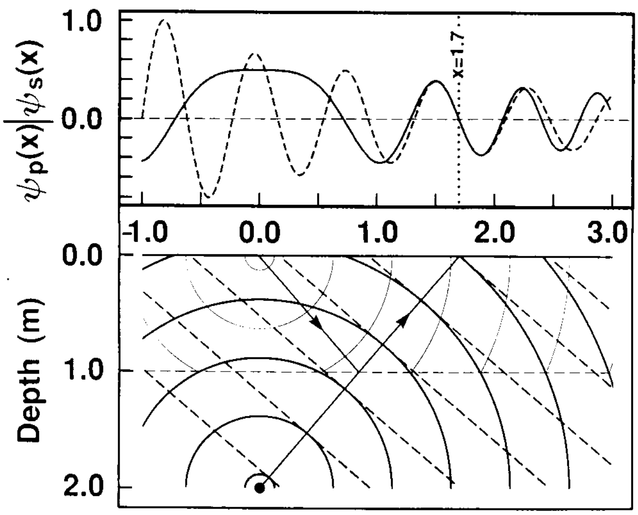

FIG. 5. Apparent waveforms arising along the x-axis in Figures 2a (solid) and 2b (dashed) with a cross-section through the associated earth model depicting plane (dashed) and spherical (solid) wavefront systems for incidence at x = 1.7 m. Reflected wavefronts emanate from an image source at z = 2.0 m associated with a point source at the origin and ideal reflection from a plane horizontal interface at z = 1.0 m.

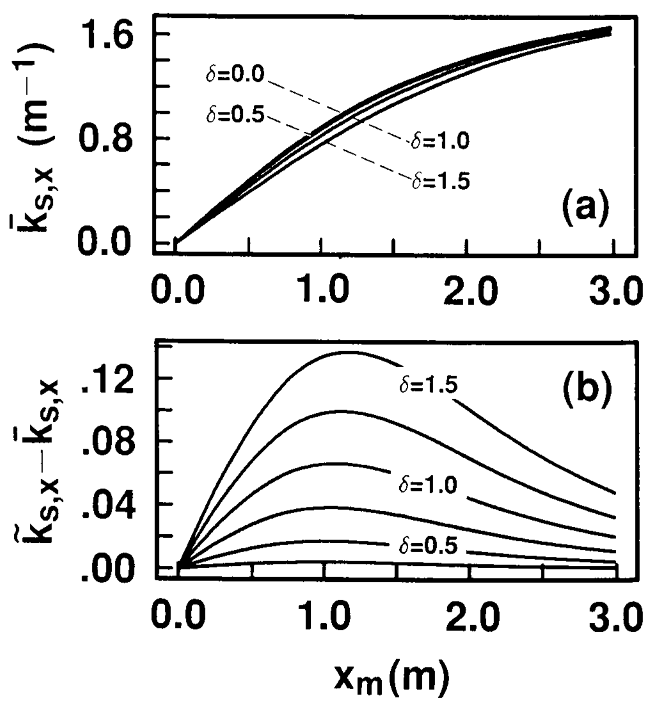

FIG. 6. (a) Comparison between local apparent wavenumber $\tilde{k}_{p,x} = \tilde{k}_{s,x}(x_m)$ at the array midpoint and average apparent wavenumber $\bar{k}_{s,x}(x_m)$ for the solid waveform displayed in Figure 5. Averages are computed for a range of half aperture values δ = 0.0–1.5 m. Note that $\tilde{k}_{p,x} = \tilde{k}_{s,x}(x_m) = \bar{k}_{s,x}(x_m)$ with δ = 0.0 m. (b) Difference between local and average apparent wavenumbers as a function of array midpoint location.

these qualifications, a useful empirical connection can be made between the average apparent wavenumber given by equation (21) and the corresponding attenuation.

In Figure 7 we display filtered waveforms resulting on application of the spatial filter characterized in Figure 4 to apparent waveforms arising at the surface for modified plane and spherical waves in Figure 5. Results are also depicted for a conventional plane wave, and array lengths are consistent with those in Figure 6. For the case $\delta = 0.25$ m, the plane wave assumption is evidently adequate as there is no appreciable difference between filtered waveforms. As array length increases, results for modified and conventional plane waves remain approximately concordant, but significant deviations arise between these and the filtered waveform for spherical incidence. In particular, in the immediate vicinity of the origin, the attenuation of spherical waves can be severe in comparison with that predicted for plane incidence. Moreover, adjacent to this near source region, a zone develops wherein the attenuation of spherical waves is appreciably less than that predicted for plane incidence. Note that the presence of this region and its extent is directly related to the difference between $\bar{k}_{s,x}(x_m)$ and $\tilde{k}_{s,x}(x_m)$ as charted in Figure 6b. Where the difference between the average apparent wavenumber and the corresponding value for plane incidence is large, the attenuation predicted assuming plane waves is too high. Beyond this region, $\bar{k}_{s,x}(x_m)$ approaches $\tilde{k}_{s,x}(x_m)$ asymptotically, and this convergence is associated with increased correlation between the filtered waveforms.

In addition, although attenuation generally increases as $\bar{k}_{s,x}(x_m)$ approaches k for large x_m, spatial aliasing becomes dominant for $\Delta x \approx \bar{\lambda}_{s,x}(x_m)$. While this effect is especially evident for $\delta = 1.5$ m in Figure 7, spatial aliasing occurs for $\delta > 0.75$ m. In particular, for $\delta = 1.0$ m, $\Delta x \approx 0.333$ so that the effective Nyquist wavenumber is $k_N = 1.5\ \text{m}^{-1}$. Consequently, according to Figure 6 ($\delta = 0$), plane waves are subject to spatial aliasing for x_m beyond about 2.25 m. Thus, for plane incidence at, say, $x_m = 3.0$ m, an apparent wavenumber of $\tilde{k}_{s,x}(3.0) \approx 1.66\ \text{m}^{-1}$ is aliased as approximately $1.34\ \text{m}^{-1}$. Of course, spherical waves are also subject to spatial aliasing but, as suggested by the positive valued difference between $\tilde{k}_{s,x}$ and $\bar{k}_{s,x}$, the onset of aliasing occurs for x_m greater than that predicted for plane incidence and thereby, in general, has lesser effect at a given x_m. For

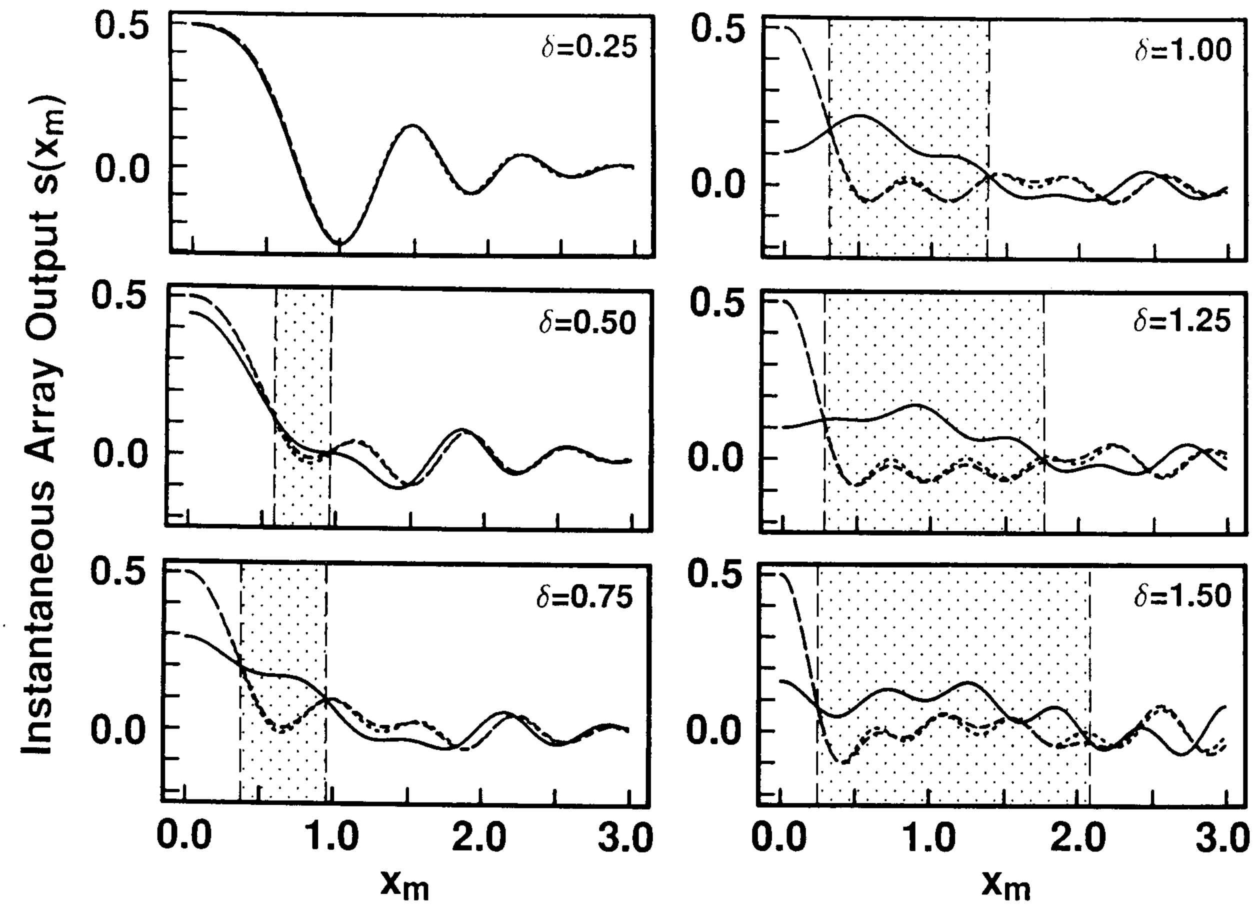

FIG. 7. Filtered apparent waveforms assuming conventional plane (dotted), modified plane (dashed), and spherical (solid) incidence. Unfiltered waveforms are depicted in Figure 5 for an array midpoint located at $x_m = 1.7$ m. Note that the apparent waveform arising for spherical wave incidence (solid) in Figure 5 remains independent of array midpoint while plane incidence waveform (dashed) varies locally. The filter's amplitude and phase spectra are displayed in Figure 4 and $\delta = 6\Delta x/2$ ranges from 0.0 to 1.5 m. Shading highlights the expanding region associated with attenuation levels consistently overestimated assuming plane incidence.

example, with $\delta = 1.0$ m, aliasing occurs for spherical waves beyond approximately 2.4 m compared with 2.25 m cited above for plane waves.

In the following section, the foregoing conclusions are substantiated by transforming the spatial array response to corresponding time-domain representations for plane and spherical incidence.

TIME-DOMAIN ARRAY FILTERS

The output of an array as a function of time can be written as the convolution

$$s(t) = a(t)*\psi(t), \tag{23}$$

where $a(t)$ is the local time-domain impulse response of the array and $\psi(t)$ is the time-dependent wave function detected at the array midpoint. The equivalent frequency-domain operation is

$$S(f) = A(f)\Psi(f), \tag{24}$$

where

$$A(f) = \int_{-\infty}^{+\infty} a(t)e^{-i2\pi ft}\, dt \tag{25}$$

is the array's transfer function and $\Psi(f)$ is the frequency-domain representation of the wave function $\psi(t)$. The array output is obtained by the inverse Fourier transform

$$s(t) = \int_{-\infty}^{+\infty} S(f)e^{i2\pi ft}\, df. \tag{26}$$

In particular, the time-domain equivalent of equation (16) can be written as

$$a(t) = \frac{1}{N}\sum_{j=-(N-1)/2}^{(N-1)/2} \alpha(j)\delta(t - t_j), \tag{27}$$

where N is the number of receiver elements and $\alpha(j)$ is an amplitude coefficient specifying the amplitude of the incident wave as detected by the jth receiver measured relative to amplitude at the array midpoint x_m. Similarly, t_j is the effective time shift of the jth detector relative to transit time measured at the array midpoint and is associated with the offset $j\Delta x$ from the midpoint in equation (16).

Assuming plane incidence, the fixed interval Δx is related to a corresponding fixed time interval Δt_p via a constant apparent horizontal phase velocity $\tilde{v}_{p,x} = f/\tilde{k}_{p,x}$, where $f = kv$ is the frequency of incident waves. Substituting equation (9) with $x_s = 0$ yields

$$\tilde{v}_{p,x} = \frac{v(x_m^2 + z_s^2)^{1/2}}{x_m} \tag{28}$$

and, thus,

$$\Delta t_p = \frac{x_m \Delta x}{v(x_m^2 + z_s^2)^{1/2}}. \tag{29}$$

Consequently, $t_j = j\Delta t_p$ in equation (27), yielding a time-domain impulse response for plane incidence that has a form resembling the corresponding spatial response except for the relative amplitude coefficient $\alpha(j)$. In fact, for a conventional plane wave, the relative amplitude coefficient is unity for all j. For spherical waves, on the other hand, the apparent velocity along the x-axis $\tilde{v}_{s,x} = f/\tilde{k}_{s,x}$ is not a constant but depends on x as

$$\tilde{v}_{s,x}(x) = \frac{v(x^2 + z_s^2)^{1/2}}{x}. \tag{30}$$

As a result, the time increment associated with the fixed interval Δx depends on j and, thus, the time interval $\Delta t_s(j)$ corresponding to a given offset $j\Delta x$ is given by

$$\Delta t_s(j) = \frac{1}{v}\int_{x_m}^{x_m + j\Delta x} \frac{x}{(x^2 + z_s^2)^{1/2}}\, dx$$

$$= \frac{1}{v}\{[(x_m + j\Delta x)^2 + z_s^2]^{1/2} - [x_m^2 + z_s^2]^{1/2}\}. \tag{31}$$

For spherical incidence, then, $t_j = \Delta t_s(j)$, yielding a time-domain impulse response having a fundamentally different form than its spatial analog.

On incorporating the appropriate relative amplitude coefficients for modified plane and spherical waves,

$$\alpha_p(j) = \frac{x_m^2 + z_s^2}{x_m^2 + x_m j\Delta x + z_s^2} \tag{32}$$

and

$$\alpha_s(j) = \left[\frac{x_m^2 + z_s^2}{(x_m + j\Delta x)^2 + z_s^2}\right]^{1/2} \tag{33}$$

respectively, the resulting array transfer functions for modified plane and spherical incidence are

$$A_p(f) = \frac{1}{N}\sum_{j=-(N-1)/2}^{(N-1)/2} \alpha_p(j)e^{-i2\pi fj\Delta t_p} \tag{34}$$

and

$$A_s(f) = \frac{1}{N}\sum_{j=-(N-1)/2}^{(N-1)/2} \alpha_s(j)e^{-i2\pi f\Delta t_s(j)}. \tag{35}$$

The difference between these transfer functions is directly related to the departure of $\tilde{\lambda}_{s,x}$ from $\tilde{\lambda}_{p,x}$ within the aperture of the array and, consequently, to the observed deviation between $\bar{k}_{s,x}(x_m)$ and $\tilde{k}_{s,x}(x_m)$ as discussed in the previous section. Amplitude and phase spectra computed from the foregoing transfer functions for $N = 7$, $\delta = 1.0$ m and $x_m =$ 0.0, 1.0, 2.0, 3.0, 5.0, and 15.0 m are displayed in Figure 8. Spectra are also depicted for conventional plane-wave incidence as given by equation (34) with $\alpha(j) = 1$. It is evident from these spectra that the filtered apparent waveforms depicted in Figure 7 for $\delta = 1.0$ m reflect changes in the array's relative amplitude and phase response for plane and spherical incidence as a function of x_m. Note that for $x_m = 0.0$ m, plane incidence implies an infinite horizontal phase velocity so that $\Delta t_p = 0.0$. Consequently, the amplitude spectra for plane incidence have unit amplitude over all frequencies, whereas the corresponding spectrum for spherical incidence is less than unity at dc and decreases with

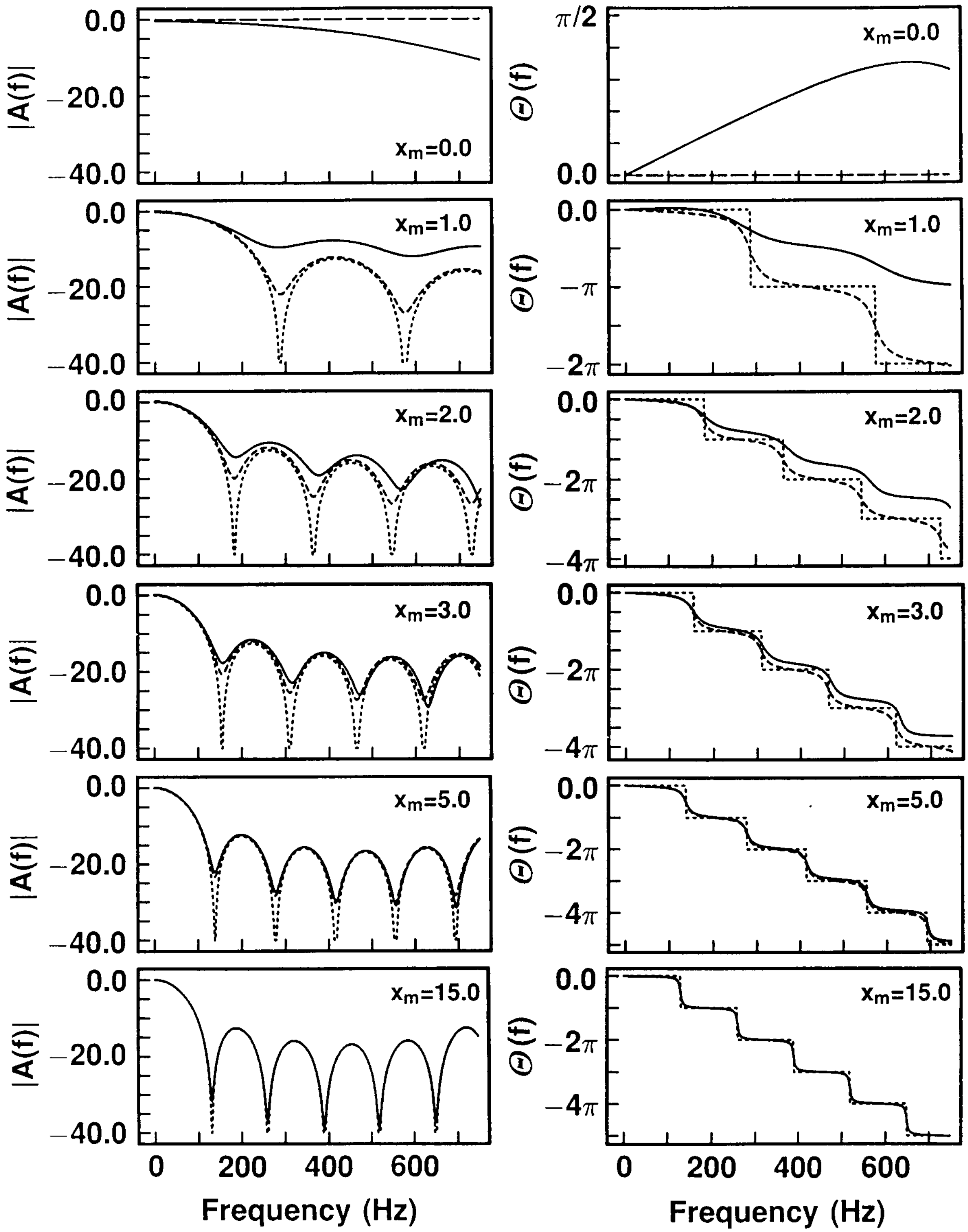

FIG. 8. Amplitude and phase spectra for time-domain array responses, assuming conventional plane (dotted), modified plane (dashed), and spherical (solid) incidence. A constant wave speed of 300.0 m/s is assumed, implying an incident wave frequency of 600 Hz. Spectra are computed with $\delta = 1.0$ m for array midpoint location of $x_m = 0.0, 1.0, 2.0, 3.0, 5.0$, and 15.0 m. Amplitude spectra are displayed on a decibel scale arbitrarily truncated at -40.0 dB. Phase angles are measured in radians.

frequency over the range depicted in Figure 8. In particular for $k = 2.0$ m^{-1} and $v = 300.0$ m/s, $f = 600.0$ s^{-1}, indicating a relative attenuation of approximately 7 dB. Spectra for $x_m = 1.0$ m are of special interest as this midpoint value resides within the zone identified in the previous section with attenuation levels that are overestimated under a plane incidence assumption. Figure 8 substantiates this finding and indicates that the spherical wave is attenuated by approximately 12 dB compared with 24 dB and 26 dB for modified and conventional plane waves, respectively. At $x_m = 2.0$ and 3.0 m, the spectra for spherical wave geometry progressively approach those predicted for plane incidence. Moreover, the amplitude spectra continue to corroborate the sense of relative attenuation observed in Figure 7. Spectra are also displayed for $x_m = 5.0$ m and 15.0 m to illustrate the continued convergence of associated array responses as the distance between the image source and array midpoint becomes large compared with the array's aperture width. It is evident from Figure 8 that the array's modified plane-wave response is intermediate between those for spherical and conventional plane waves. Interestingly, it is also apparent that the spherical wave response converges more rapidly toward the modified plane-wave response than either of these converge with the response for a conventional plane wave. This observation is best illustrated by displaying the corresponding complex transfer functions in polar format as in Figure 9. By nature, the imaginary part of the transfer function for conventional plane waves is identically zero and, consequently, corresponding phasor diagrams reside on the real axis. Concurrently, the real component takes on the frequency-dependent value $\sin(N\pi f\Delta t_p)/N\sin(\pi f\Delta t_p)$. As this quantity changes sign, the corresponding phasor diagram passes through the origin and the associated phase spectrum in Figure 8 jumps by $-\pi$ radians. In fact, theoretically, these phase discontinuities can take on an arbitrary value $\pi \pm n2\pi$ radians but a constant decrement of π radians is both physically plausible and consistent with phasor diagrams for modified plane and spherical waves. Note that the phase spectra displayed in Figure 8 for modified plane and spherical wave have been corrected for meaningless wraps of 2π radians introduced computationally as the respective phasor diagrams cross the negative valued real axis. Convergence of the complex array response for spherical incidence to that for modified plane waves reflects the significant influence of relative amplitude variation over the array's aperture.

Despite the insight gained by treating the receiver array as a time-domain filter, we should not lose sight of the fact that the array is physically deployed in the spatial domain and affects a discrete sampling of the spatial wavefield while

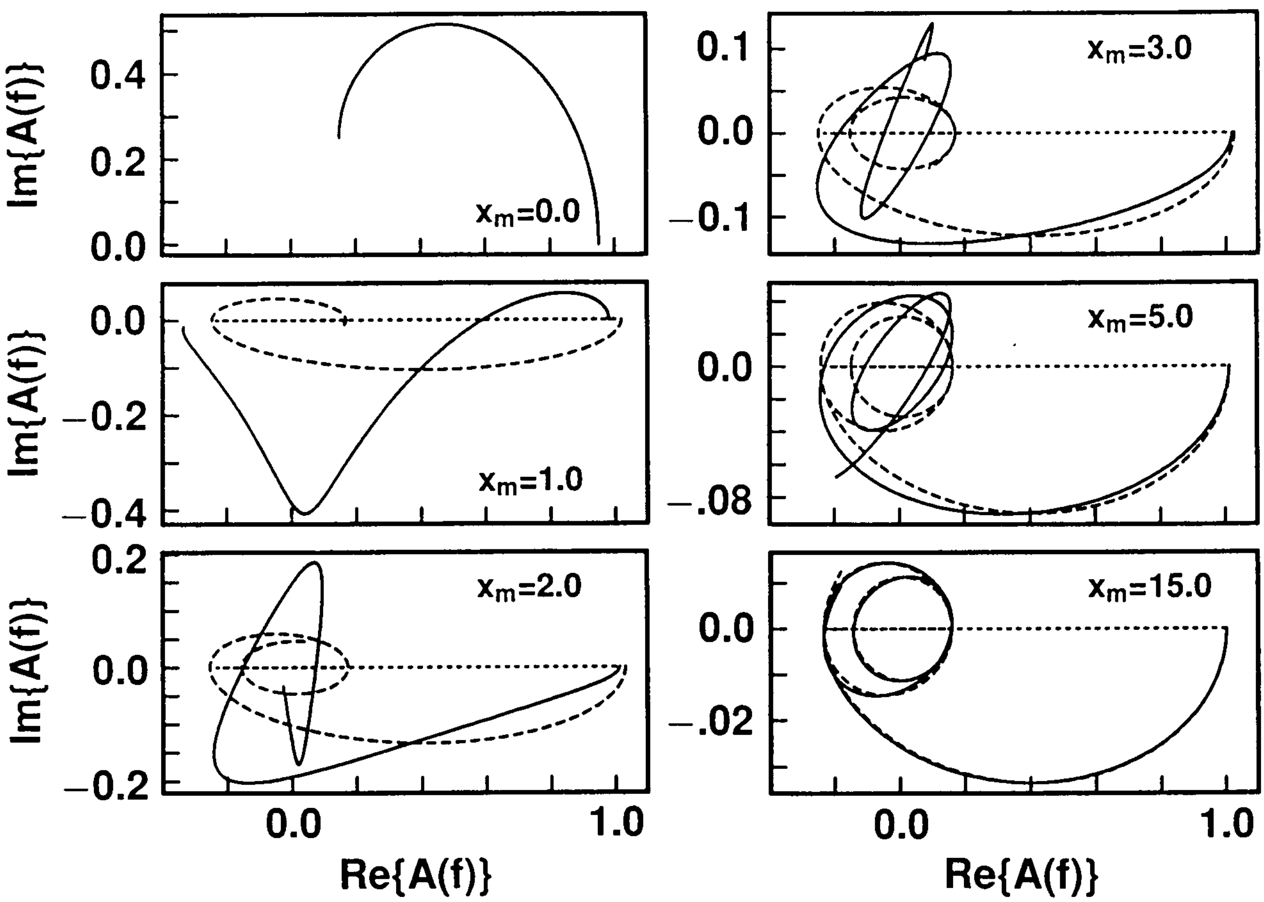

FIG. 9. Polar diagrams characterizing the complex transfer functions associated with the corresponding amplitude and phase spectra in Figure 8 for conventional plane (dotted), modified plane (dashed), and spherical (solid) incidence. Real and imaginary components of a complex transfer function $A(f)$ are denoted by $Re\{A(f)\}$ and $Im\{A(f)\}$, respectively.

responding continuously in time. Consequently, while an appropriate Nyquist wavenumber is associated with the spatial interval separating adjacent elements of the array, the time-domain analogue is not a Nyquist frequency in the usual sense. Only subsequently, on digitizing the array's analog output, does the possibility of temporal aliasing and, thus, a Nyquist frequency arise. Having made this distinction, however, it is useful to consider the time-domain analogue of the Nyquist wavenumber associated with the spatial filter. We shall refer to this parameter as the pseudo-Nyquist frequency.

For plane incidence, a pseudo-Nyquist frequency f_N is associated with the Nyquist wavenumber by

$$f_{N,p}(x_m) = k_N \bar{v}_{p,x}(x_m) = \frac{v k_N}{x_m} (x_m^2 + z_s^2)^{1/2}, \tag{36}$$

where $\bar{v}_{p,x}(x_m)$ is the apparent plane-wave velocity relating the constant spatial interval Δx, separating adjacent detectors, with the constant temporal interval Δt_p. Using $k_N = 1.5\ \mathrm{m}^{-1}$ from the previous section, effective pseudo-Nyquist frequencies for $\delta = 1.0$ m at $x_m = 0.0$, 1.0, 2.0, and 3.0 m are, respectively, ∞, 1000, 640, and 540 s^{-1}. Consequently, aliasing occurs only for the case $x_m = 3.0$ m where the incident wave frequency $f = 600\ \mathrm{s}^{-1}$ aliases at approximately 480 s^{-1}. More specifically, equation (36) confirms that the onset of aliasing occurs at approximately $x_m = 2.25$ m.

For spherical incidence, the effective time interval between successive array elements is nonconstant and, consequently, it is impossible to define a unique pseudo-Nyquist frequency. Instead, in analogy with the average apparent wavenumber considered in the previous section, we introduce an average pseudo-Nyquist frequency

$$\begin{aligned}\bar{f}_{N,s}(x_m) &= k_N \bar{v}_{s,x}(x_m) \\ &= \frac{v k_N}{2\delta} \Bigg\{ [(x_m + \delta)^2 + z_s^2]^{1/2} - [(x_m - \delta)^2 + z_s^2]^{1/2} \\ &\quad + z_s \ln \left[\frac{(x_m + \delta)}{(x_m - \delta)} \left(\frac{z_s + [(x_m - \delta)^2 + z_s^2]^{1/2}}{z_s + [(x_m + \delta)^2 + z_s^2]^{1/2}} \right) \right] \Bigg\},\end{aligned} \tag{37}$$

where

$$\bar{v}_{s,x}(x_m) = \frac{1}{2\delta} \int_{x_m - \delta}^{x_m + \delta} \bar{v}_{s,x}(x)\, dx$$

is the average apparent velocity as depicted in Figure 10. A computational comparison of equations (36) and (37) suggests that, in general, the onset of aliasing occurs at a higher frequency than predicted for plane incidence. This is illustrated in Figure 10, where it is observed that $\bar{v}_{s,x}(x_m)$ always exceeds $\bar{v}_{p,x}(x_m)$. The average pseudo-Nyquist frequencies associated with these average apparent velocities are obtained by a constant scaling with the appropriate Nyquist wavenumber. Note that for $-\delta \le x_m \le \delta$ the argument of the logarithm in equation (37) is negative, causing the average pseudo-Nyquist frequency to be undefined. Physically, this result reflects inclusion of $x = 0$, where $\lim_{x \to 0} \bar{v}_{s,x}(x) = \infty$, within the aperture of the array so that the average pseudo-Nyquist frequency over this region must also be infinite.

CONCLUDING DISCUSSION

The foregoing analysis identifies theoretical limitations on the plane wave assumption normally invoked when characterizing the attenuation properties of receiver arrays. While the array's spatial response is uniquely defined by the number of elements, their relative weighting and spatial distribution, equivalent time-domain representations necessarily incorporate the geometry and spatial amplitude dependence of incident wavefronts. Consequently, as demonstrated above, distinct time-domain impulse responses arise in connection with plane and spherical incidence. Moreover, we find that this distinction is manifest spatially as a systematic difference between the spectral compositions of associated waveforms within the array's aperture. Although both perspectives reveal that attenuation predicted assuming plane incidence can deviate appreciably from that experienced by a spherical wave, the practical significance of these deviations is difficult to appraise.

Newman and Mahoney (1973) examined the influence of random implementation errors on the nominal response of uniform, linear tapered, and optimally weighted line arrays. Practical uncertainty and error in the effectiveness, position, and coupling of individual array elements was modeled by introducing random perturbations of 10 percent standard deviation about their nominal spatial distribution and weighting. While resulting deviations from the nominal response were found to be insignificant within the passband, perturbations had an appreciable effect beyond the first notch in the amplitude response, imposing a practical limitation on the rejection capabilities of the array. Newman and Mahoney also acknowledged errors in design assumptions, including the simplifying assumption of plane-wave incidence, and suggested that such errors could be treated as equivalent implementation errors. For example, the re-

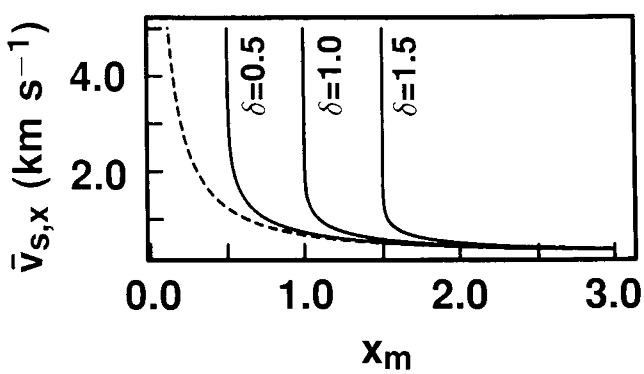

FIG. 10. Average apparent velocity for plane (dashed) and spherical (solid) incidence. Averages are depicted for half apertures of $\delta = 0.5$, 1.0, and 1.5 m. Note that the plane incidence value is equivalent to the average apparent spherical wave velocity for $\delta = 0.0$ m. All curves approach infinity as x_m approaches δ and are arbitrarily truncated at 5.0 km/s for the purpose of illustration.

sponse of a uniform line array to spherically incident waves can be simulated, while retaining the plane-wave assumption, by redistributing individual elements on the appropriate arc of radius in the x-z plane and assigning variable weighting coefficients to account for spherical divergence. Inversely, by determining the magnitude of required departures from a uniform line array, we can assess the relative significance of deviations from the plane-wave assumption compared with typical implementation errors.

In Figure 11a, the relative deviations of amplitude coefficient, $\alpha_s(j)$ and the effective time shift $\Delta t_s(j)$ from the respective values of unity and $j\Delta t_p$ for conventional plane-wave incidence are displayed as a function of element position for array midpoints of 0.0, 1.0, 2.0, and 3.0 m. Two important observations are made. First, the maximum effective errors are significantly larger than the 10 percent perturbations assumed by Newman and Mahoney for typical implementation errors, indicating that for small scale, near-source applications, implementation errors have a relatively minor influence compared with departures from design assumptions. Second, while implementation errors become dominant with increasing distance from the source, it is interesting to note that effective time-lag errors diminish rapidly compared with relative amplitude deviations. In other words, although spherical wavefronts may be reasonably approximated as locally plane at a given range from the source, spherical divergence can remain a significant factor. Note that this observation and the comparatively minor deviation between relative amplitude coefficients $\alpha_s(j)$ and $\alpha_p(j)$, illustrated in Figure 11b, are consistent with the relatively rapid convergence of time-domain array responses for spherical and modified plane waves in the previous section. It is emphasized, however, that despite a significant reduction in relative amplitude deviation, relative time-lag errors are identical in Figures 11a and 11b, reflecting a fundamental limitation of any plane wavefront approximation.

The foregoing observations can be generalized for an arbitrary midpoint offset, image source depth, and aperture width in terms of two non-negative, dimensionless parameters $\sigma_\Delta = \delta/x_m$ and $\sigma_z = z_s/x_m$. Defining relative amplitude deviations as

$$\varepsilon_{\alpha p} = \alpha_s(j) - 1 \tag{38}$$

and

$$\varepsilon_{\alpha m} = \frac{\alpha_s(j) - \alpha_p(j)}{\alpha_p(j)} \tag{39}$$

for plane and modified plane-wave approximations, respectively, the relative time-lag deviation by

$$\varepsilon_t = \frac{\Delta t_s(j) - j\Delta t_p}{j\Delta t_p} \tag{40}$$

and assuming a three-element array, so that maximum deviations occur for $j = \pm(N - 1)/2$, we obtain the corresponding nondimensionalized expressions for maximum relative deviation

$$\hat{\varepsilon}_{\alpha p} = \left|\left(\frac{1 + \sigma_z^2}{1 \pm 2\sigma_\Delta + \sigma_\Delta^2 + \sigma_z^2}\right)^{1/2} - 1\right|, \tag{41}$$

$$\hat{\varepsilon}_{\alpha m} = \left|\frac{(1 \pm \sigma_\Delta + \sigma_z^2)(1 + \sigma_z^2)^{-1/2}}{(1 \pm 2\sigma_\Delta + \sigma_\Delta^2 + \sigma_z^2)^{1/2}} - 1\right|, \tag{42}$$

$$\hat{\varepsilon}_t = \left|\frac{1}{\pm\sigma_\Delta}\left[\frac{(1 \pm 2\sigma_\Delta + \sigma_\Delta^2 + \sigma_z^2)^{1/2}}{(1 + \sigma_z^2)^{-1/2}} - (1 + \sigma_z^2)\right] - 1\right|. \tag{43}$$

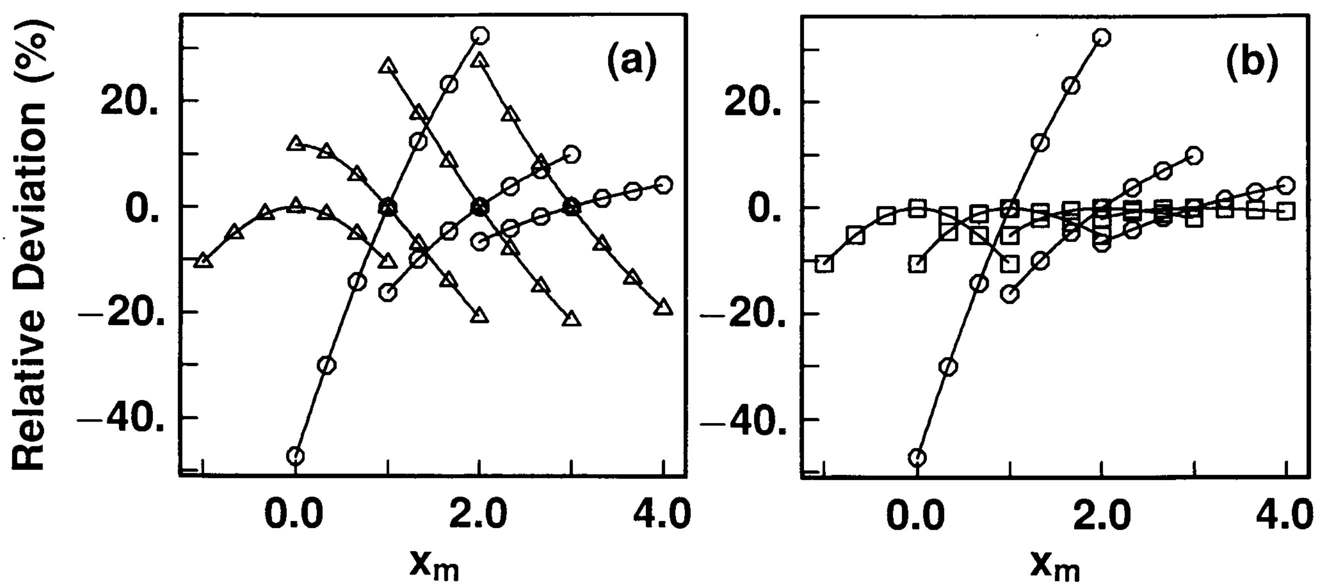

FIG. 11. Relative deviation of amplitude coefficient $\alpha_s(j)$, and effective time lag $\Delta t_s(j)$ from (a) conventional plane-wave values: $\Delta = (\alpha_s(j) - 1)$, ○ = $[(\Delta t_s(j)/j\Delta t_p) - 1]$, and (b) modified plane-wave values: □ = $[(\alpha_s(j)/\alpha_p(j)) - 1]$, ○ = $[(\Delta t_s(j)/j\Delta t_p) - 1]$. Solid curves connect discrete values for a seven element array deployed with midpoints at 0.0, 1.0, 2.0, and 3.0 m. The image source is located x = 0.0 m, z = 2.0 m.

In fact, geometrical analysis indicates that except for $\hat{\varepsilon}_{\alpha s}$ when $j < 0$ and $1 < \sigma_\Delta < \{1 + 2(1 + \sigma_z^2)^{1/2}[1 - \sigma_z(1 + \sigma_z^2)^{-1/2}]^{1/2}\}$, the foregoing expressions are valid for arbitrary N as illustrated below.

Figures 12b and 13b display $\hat{\varepsilon}_{\alpha p}(\Delta)$ and $\hat{\varepsilon}_{\alpha m}(\square)$, respectively, for $j = (N - 1)/2$ together with the associated relative time-lag deviation $\hat{\varepsilon}_t(\bigcirc)$ as functions of the dimensionless parameters σ_Δ and σ_z. The contour interval is 5 percent. Corresponding distributions for $j = -(N - 1)/2$ in Figures 12a and 13a are more complicated due to singularities in the relative amplitude coefficients $\alpha_p(j)$ and $\alpha_s(j)$ defined by equations 32 and 33, respectively. In particular, for an image source at the surface ($\sigma_z = 0$) and an aperture width equal to twice the midpoint offset ($\sigma_\Delta = 1$), the $j = -(N - 1)/2$ detector coincides with the source causing the amplitude coefficient for spherical incidence to be infinite. The same situation arises for the modified plane-wave coefficient, however, in this case a similar condition occurs for

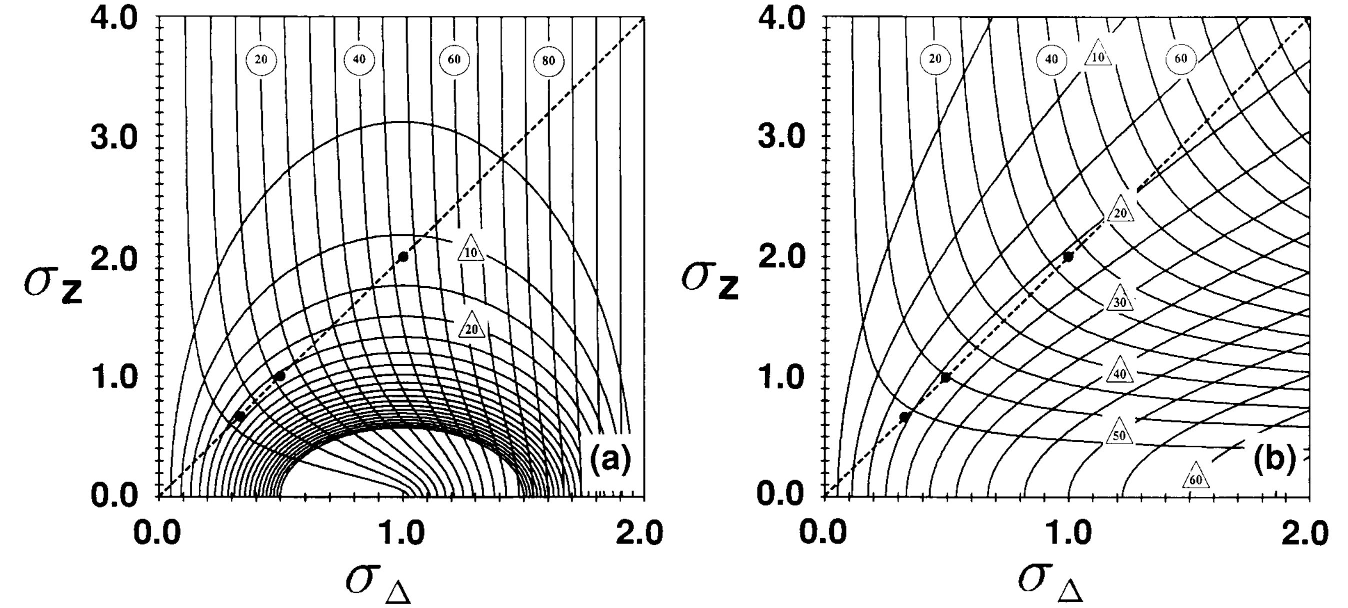

FIG. 12. Maximum relative amplitude (Δ) and time-lag ($\bigcirc$) deviations from conventional plane-wave values as functions of dimensionless parameters $\sigma_\Delta = \delta/x_m$ and $\sigma_z = z_s/x_m$ for (a) $j = -(N - 1)/2$ and (b) $j = (N - 1)/2$. Discrete mappings are depicted for $z_s = 2.0$ m, $\delta = 1.0$ m and $x_m = 1.0$, 2.0, and 3.0 m. Compare predicted errors with Figure 11a.

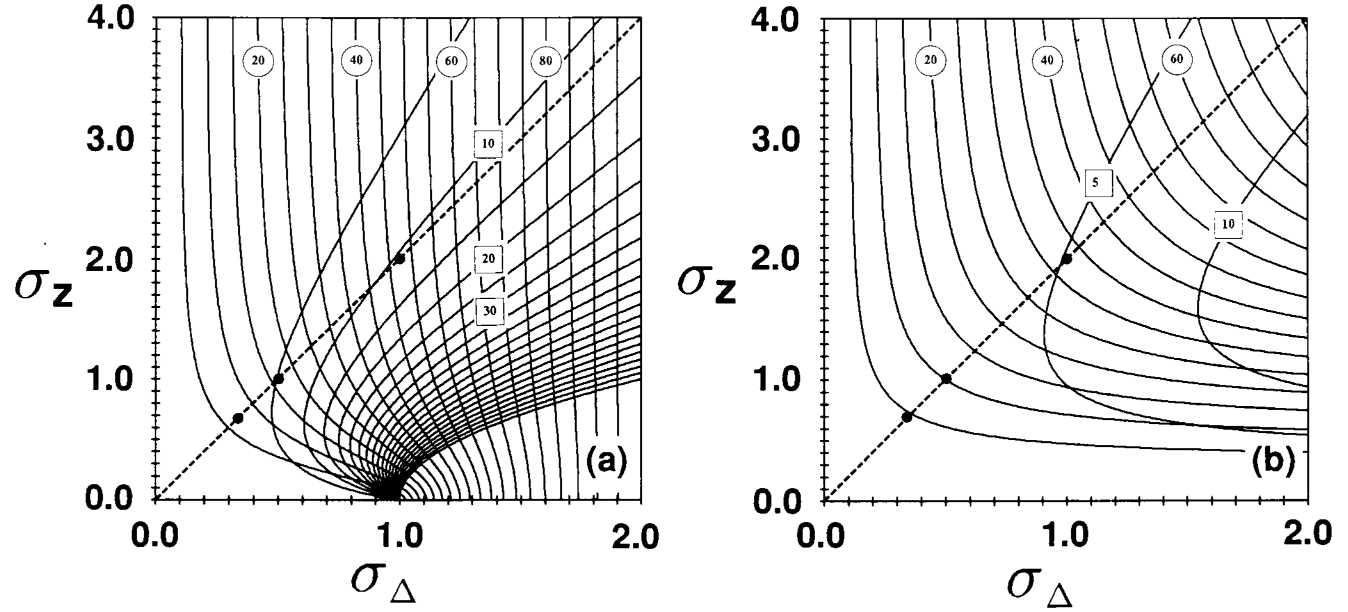

FIG. 13. Maximum relative amplitude ($\square$) and time-lag ($\bigcirc$) deviations from modified plane-wave values as functions of dimensionless parameters $\sigma_\Delta = \delta/x_m$ and $\sigma_z = z_s/x_m$ for (a) $j = -(N - 1)/2$ and (b) $j = (N - 1)/2$. Discrete mappings are depicted for $z_s = 2.0$ m, $\delta = 1.0$ m and $x_m = 1.0$, 2.0, and 3.0 m. Compare predicted errors with Figure 11b.

all σ_z satisfying $\sigma_z = \sqrt{\sigma_\Delta - 1}$. It is evident from equation (39) that $\lim_{\alpha p(j) \to \infty} \varepsilon_{\alpha m} = -1$ and, consequently, this condition corresponds to the $\hat{\varepsilon}_{\alpha m} = 100$ percent contour in Figure 13a. Finally, Figure 14 is a hybrid of Figures 12a and 12b, depicting the overall maximum deviation as a function of σ_Δ and σ_z. For the modified plane-wave approximation, relative deviations are always maximum for $j = -(N - 1)/2$.

To illustrate the systematics of these generalized error distributions, we return to the specific example illustrated above (Figure 11). Fixing $z_s = 2.0$ m and $\delta = 1.0$ m, array midpoint offsets of 1.0, 2.0, and 3.0 m have one to one mappings $(\sigma_\Delta, \sigma_z) = (1.0, 2.0)$, $(0.5, 1.0)$, and $(0.33, 0.67)$, respectively. As illustrated in Figures 12–14, these points define a line having slope $z_s/\delta = 2.0$ and passing through the origin. Moreover, as the midpoint offset increases, its mapping approaches the origin and, in general, this trend is accompanied by a reduction in associated relative deviations. In particular, Figure 14 indicates that the relative time-lag error becomes less than 10 percent for $\sigma_\Delta = \delta/x_m < 0.4$ or $x_m > 2.5$ m. Concurrently, in agreement with previous observations, the relative amplitude deviation diminishes less rapidly falling to 10 percent in this case at approximately $\sigma_\Delta = 0.1$ or $x_m = 10$ m. On the other hand, for an arbitrary value of σ_Δ, increasing σ_z, or effectively increasing the image source depth, generally reduces relative amplitude deviations more rapidly than relative time-lag deviations. Indeed, as expected for an image source at infinite depth, the corresponding line on Figures 12–14 has infinite slope and consequently resides on the ordinate axis where all relative deviations vanish.

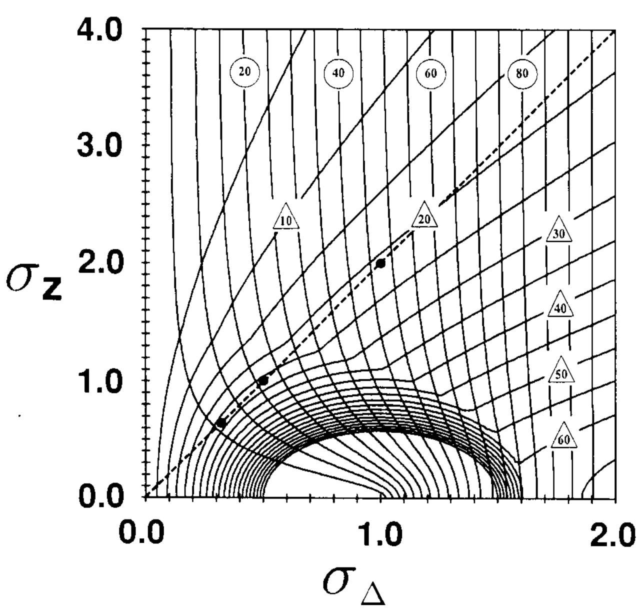

FIG. 14. Composite of Figures 12a and 12b, displaying overall maximum deviations from corresponding conventional plane-wave values. Note that Figure 13a is the equivalent distribution relative to corresponding modified plane-wave values.

In general, the foregoing error analysis reveals that the magnitude of effective implementation errors required to compensate an inappropriate plane-wave assumption are primarily controlled by the ratio of reflector depth to aperture width. Moreover, relative amplitude and time-lag deviations diminish at rates governed by the previous parameter as the array's midpoint offset becomes large, compared with both reflector depth and aperture width. Finally, as demonstrated by Newman and Mahoney (1973), the response of the uniform array is least influenced by implementation errors and, consequently, departures from design assumptions, including plane incidence. As a result, relative errors arising from a plane-wave approximation are significantly magnified in the case of optimally weighted arrays.

In closing, it is noted that this investigation was partly motivated by suspicion that the viability of array filtering for ground roll attenuation in small-scale seismology might have been inappropriately dismissed on the basis of a plane-wave assumption. Knapp and Steeples (1986) sought to maximize array length subject to attenuating the highest signal frequency by less than 3 dB and although not explicitly stated, subsequent analysis assumed plane incidence, concluding that $\delta_{\max} = 0.125/\bar{k}_{\max}(z_s/2) \sim 0.28/k_{\max}$, where the argument $z_s/2$ implies that maximum offset is taken equal to reflector depth. In a related discussion, Mayne (1987) confirmed the foregoing result for a two-element array and noted that for an array having a large number of elements, the correct relation is $\delta_{\max} \sim 0.48/k_{\max}$. From Figure 4, for example, we note that the corresponding relation for a seven-element array is $\delta_{\max} \sim 0.43/k_{\max}$. Although $\delta_{\max}$ *can* be theoretically underestimated assuming plane incidence, frequency-domain analysis, using equations (34) and (35) with $f = f_{\max}$ and Δt_p evaluated for $x_m = z_s/2$, indicates that the effect is negligible for a wide range of plausible field parameters. Consequently, the present study supports the validity of a plane-wave assumption in this context and reinforces the conclusion that array filters are not optimally suited for small scale applications. This does *not*, however, exclude the use of spatial filtering, and it is emphasized that where less stringent performance criteria are accepted, the deviations between spherical and plane-wave response functions can be significant, particularly over the reject band. In conclusion, although plane incidence remains a useful working assumption for smaller scale seismic applications, some measure of sober second thought is warranted.

REFERENCES

Dobrin, M. B., 1976, Introduction to geophysical prospecting, third edition: McGraw-Hill Book Co. Inc.

Holzman, M., 1963, Chebyshev optimized geophone arrays: Geophysics, **28**, 145–155.

Knapp, R. W., and Steeples, D. W., 1986, High-resolution common-depth-point reflection profiling: Field acquisition parameter design: Geophysics, **51**, 283–294.

Mayne, W. H., 1987, High-resolution common-depth-point reflection profiling: Field acquisition parameter design (Discussion): Geophysics, **52**, 2011.

Newman, P., and Mahoney, J. T., 1973, Patterns-with a pinch of salt: Geophys. Prosp., **21**, 197–219.

Parr, J. O., and Mayne, W. H., 1955, A new method of pattern shooting: Geophysics, **20**, 539–560.